NANO LETTERS



pubs.acs.org/NanoLett
Letter

# Phonon-Dominated In-Plane Thermal Conductivity of Single-Flake Metallic $Ti_3C_2T_x$ MXene

Max C. van Hemert, Hugh Ramsden, Stefano Ippolito, Sebin Varghese, Bohai Liu, Elvira Tornero Gasca, Miguel Muñoz Rojo, Hai I. Wang, Yury Gogotsi, and Klaas-Jan Tielrooij*

Cite This: https://doi.org/10.1021/acs.nanolett.6c01850



**ABSTRACT:** MXenes are a promising class of 2D materials, with prospects in applications such as electromagnetic interference shielding, energy storage, catalysis, and thermal management. Despite the importance of understanding their thermal transport properties, it is not clear whether electrons or phonons dominate heat transport, and the experimentally obtained in-plane thermal conductivities vary substantially. Here, we address this by studying in-plane heat transport in single $Ti_3C_2T_x$ MXene flakes using spatiotemporal microscopy, directly visualizing heat transport in space and time. We obtain a thermal diffusivity of 0.05 $cm^2\ s^{-1}$, corresponding to an in-plane thermal conductivity of 13−16 W $m^{-1}\ K^{-1}$. Using an upper limit for the electronic conductivity based on terahertz measurements, we find that electrons carry at most half of the heat. This shows that—despite their metallic nature—phonons play an important role in the heat transport of $Ti_3C_2T_x$ MXene, providing an unconventional combination of heat and charge transport properties.

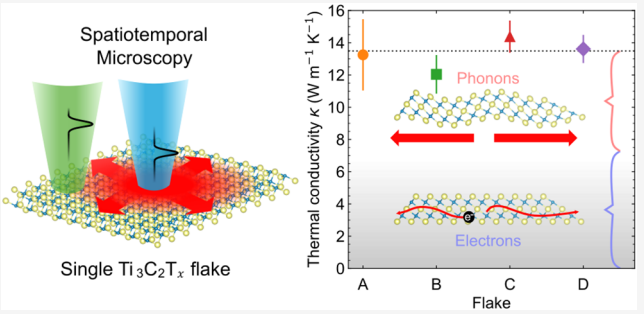


**KEYWORDS:** *MXene, heat transport, 2D materials, optothermal, spatiotemporal microscopy, $Ti_3C_2T_x$*

MXenes are a family of layered materials comprising molecularly thin layers of transition-metal carbides, nitrides, or carbonitrides, which are typically terminated by hydrophilic surface groups.[1,2] Examples are titanium nitride, $Ti_4N_3T_x$, molybdenum carbide, $Mo_2CT_x$, and titanium carbide, $Ti_3C_2T_x$, where $T_x$ represents mixed-termination groups, typically O, Cl, F, or OH. These materials are receiving increasing attention due to their interesting fundamental physical properties and their potential in a wide range of applications,[3,4] including energy storage,[5,6] thermal management,[7] electromagnetic interference shielding,[8] and sensing,[9,10] while offering scalable synthesis routes, such as top-down etching and chemical vapor deposition.[4,11,12] For these materials to see widespread use, it is important to understand their fundamental properties, including their thermal conductivity.[13]

There are currently two important open questions regarding in-plane heat transport of the most-studied and practically important MXene $Ti_3C_2T_x$. First, the fundamental question of whether electrons or phonons dominate in-plane heat transport remains unanswered. Since this material has a metallic band structure,[14−16] and heat conduction in metals typically occurs via electrons, electronic heat transport is expected to dominate over phononic heat transport. However, some previous studies point at phonon-dominated heat transport,[17,18] while others point at electron-dominated transport.[19] Second, the experimentally reported values for the in-plane thermal conductivity of $Ti_3C_2T_x$ vary significantly: from below 1 W $m^{-1}\ K^{-1}$ to 55 W $m^{-1}\ K^{-1}$.[17−23] An explanation for these inconsistent values may be that most previous studies have focused on a thin film geometry with many partially overlapping flakes.[17,18,20] This creates challenges in probing intrinsic transport properties, as these measurements are sensitive not only to the intrinsic thermal conductivity but also to other factors, such as the flake size and thickness, the interflake thermal resistance,[17] temperature,[24] and the environmental humidity.[21] Furthermore, MXenes are predicted to exhibit anisotropic thermal conductivity,[25,26] which means that an experimental method is required that enables unambiguous decoupling of in- and out-of-plane thermal transport.

Here, we address these issues by studying the in-plane heat transport of individual $Ti_3C_2T_x$ MXene flakes using spatiotemporal differential reflection microscopy. As illustrated in Figure 1a, spatiotemporal microscopy[27−30] allows us to follow

Received: April 16, 2026
Revised: July 20, 2026
Accepted: July 23, 2026





https://doi.org/10.1021/acs.nanolett.6c01850
Nano Lett. XXXX, XXX, XXX−XXX

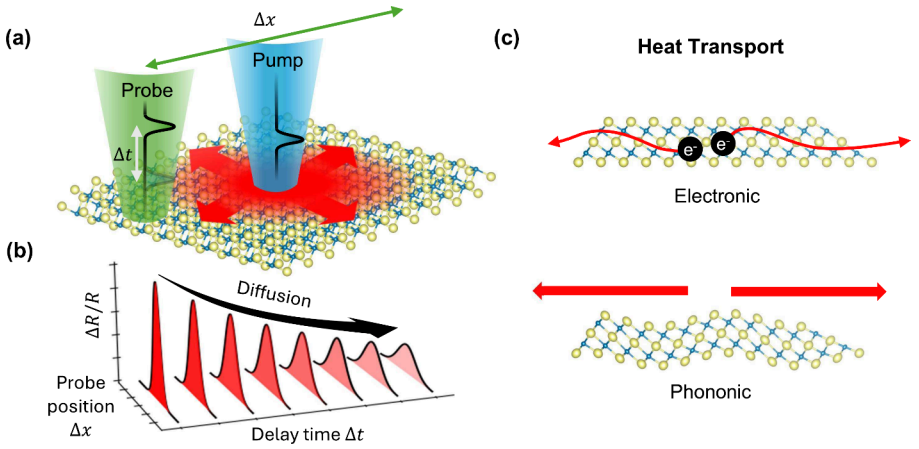


**Figure 1.** Spatiotemporal microscopy of heat transport by phonons and electrons. **a.** Schematic illustration of the principle of spatiotemporal microscopy to study in-plane heat transport. A pump pulse (blue) heats the central part of single-flake MXene. The heat (red) diffuses outward and a pump-induced reflectivity change $\Delta R/R$ is measured by the probe pulse (green) due to the temperature-dependent reflectivity around the plasmon resonance. The probe is offset relative to the pump in space and time by $\Delta x$ and $\Delta t$, respectively. Spatiotemporal profiles are collected by scanning the probe in space and time. **b.** Evolution of the heat profile measured by spatiotemporal microscopy. Initially the profile matches that of the Gaussian-shaped pump pulse. With increasing $\Delta t$, diffusion causes this to spread out. **c.** Illustration of two different carriers of heat: electrons (top) and phonons (bottom).

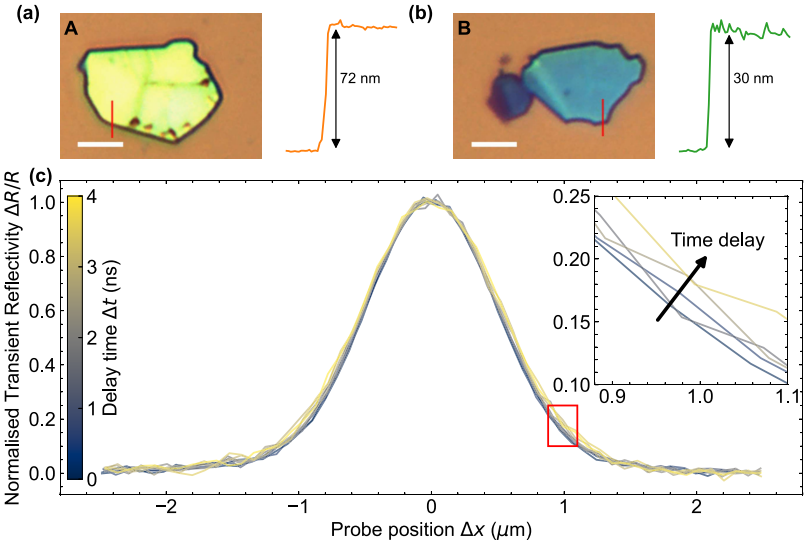


**Figure 2.** Spatiotemporal measurements of in-plane heat transport. **a,b.** Optical images together with AFM line traces for flake A (**a**) and flake B (**b**). The scale bars are 5 $\mu$m. **c.** Spatial transient reflectivity profiles $\Delta R/R$ of flake D, as a function of spatial pump−probe offset $\Delta x$, for five different time delays $\Delta t$ between 0 and 4 ns (see color bar). These profiles correspond to spatial temperature profiles. The broadening of the profiles with time delay—due to heat transport—is on the order of tens of nanometers, as visible in the inset on the right.

diffusion directly in space and time by examining the spatial broadening of an initial localized photoexcitation, shown in Figure 1b. In this way, we exclusively observe the in-plane diffusion of heat. This is a local technique where the initial optically pumped region has a diameter of around one micrometer, which is smaller than the typical flake size. Using an optical probe, we resolve transport-induced spatial broadening with a precision below 10 nanometers. This allows us to study individual $Ti_3C_2T_x$ flakes and therefore obtain intrinsic heat diffusion properties. Moreover, because we directly observe heat transport in space and time, we obtain the thermal diffusivity without the need for prior knowledge of material parameters. We assess the contribution of electrons vs phonons to heat transport (see Figure 1c) using the microscopic charge conductivity obtained through all-optical electronic transport measurements.[31] Our results show that—unlike in a typical metal—phonons play an important role in carrying in-plane heat in $Ti_3C_2T_x$ MXene flakes.

The MXene flakes were synthesized by wet-chemical etching from the $Ti_3AlC_2$ MAX phase (as described in refs 26 and 32) and deposited onto $Si/SiO_2$ substrates, starting from extremely dilute dispersions (0.01 to 0.001 mg/mL). From this, we obtained isolated MXenes flakes, allowing us to measure their intrinsic in-plane heat transport properties. We chose four specific flakes for our transport measurements, labeled flakes A, B, C, and D, which were chosen based on their size and uniformity. Atomic force microscopy (AFM) measurements showed that these flakes have thicknesses from 30 to 70 nm, while optical images showed lateral sizes varying between 5 and 20 $\mu$m (see Figures 2a,b and Supplementary Figure 6). We note that thermoreflectance measurements[26] and scanning thermal microscopy measurements[19] on identical $Ti_3C_2T_x$


https://doi.org/10.1021/acs.nanolett.6c01850
Nano Lett. XXXX, XXX, XXX−XXX

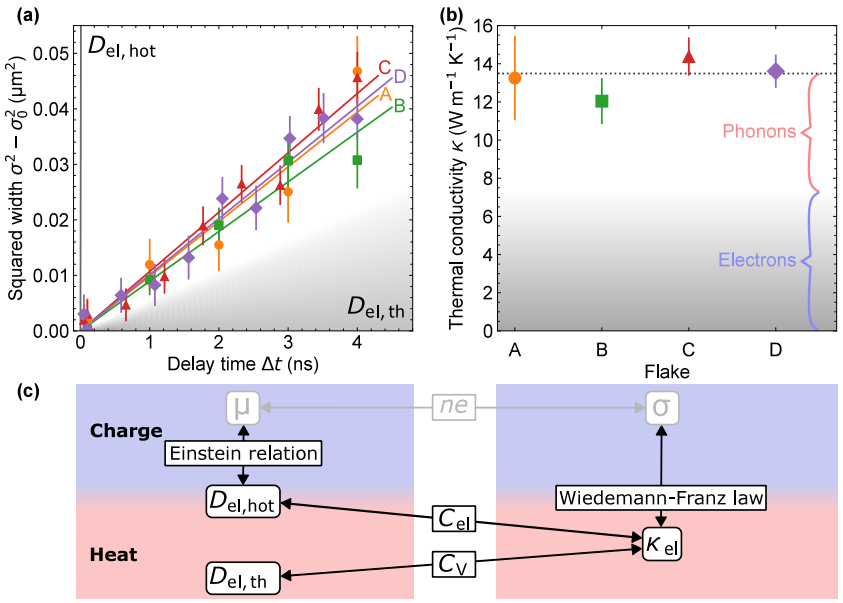


**Figure 3.** In-plane thermal diffusivity and conductivity. **a.** The change in squared width $\sigma^2-\sigma_0^2$, obtained by describing the spatial profiles in Figure 2c and Figure 7 of the Supporting Information by a Gaussian function with standard width $\sigma$, as a function of time delay $\Delta t$ for four different flakes. The slope is directly proportional to the thermal diffusivity $D$. The expected evolution of the squared width for diffusion of hot electrons $D_{el,hot}$, before thermalization between electrons and phonons has occurred, is almost parallel to the vertical axis. The shaded area represents the expected evolution of the squared width for purely electronic heat transport after electrons and phonons have thermalized $D_{el,th}$, for a range of different conductivities. The upper-bound is based on the microscopic charge conductivity obtained by terahertz transport measurements from ref 31, the application of Wiedemann−Franz law, and division by the heat capacity $C_V$ from ref 26. **b.** The heat conductivity calculated by multiplying the obtained diffusivities for the different flakes, by the heat capacity $C_V$ with the weighted average (dotted line). The braces show the contributions from electrons and from phonons to the heat transport, indicating the importance of phonons for in-plane heat transport. **c.** Schematic showing how microscopic and macroscopic properties describing heat and charge transport are connected. In particular, the electrical conductivity and mobility are related via the carrier density $n$, electron charge $e$, and the charge mobility $\mu$, while the diffusivity of hot electrons $D_{el,hot}$ and of thermalized electrons $D_{el,th}$ are related to the electronic contribution to the thermal conductivity via the heat capacity.

flakes showed highly inefficient out-of-plane heat transport to the substrate. Performing pump−probe measurements with varying laser repetition rate, similar to ref 31, allows us to estimate the out-of-plane heat flux, which is indeed low: 3.2−5.4 MW m$^{-2}$ K$^{-1}$ (see Supplementary Note 5). Therefore, it was not necessary to suspend the flakes, as was done in previous spatiotemporal heat transport measurements of 2D materials.[29] For further details on the sample preparation and characterization, see Supplementary Notes 1 and 2.

We used spatiotemporal differential reflection microscopy[27−30] to study heat transport. In this technique, illustrated in Figure 1a, a focused pump pulse with a duration of 50 ps and a wavelength of 590 nm locally photoexcites the center of a MXene flake. We then measure the pump-induced reflectivity change $\frac{\Delta R}{R}$ using a time-delayed probe pulse with a duration of 30 ps and a wavelength of ∼750 nm. At this wavelength, the reflectivity is governed by a temperature-dependent plasmon resonance[33−35] of $Ti_3C_2T_x$, and we operate in the regime where the signal scales linearly with pump and probe fluences (see Figures 3 and 4 of the Supporting Information). Therefore, scanning the probe beam over the pump spot, we obtain transient reflectivity profiles, which give the spatial distribution of the temperature change induced by the pump. As illustrated in Figure 1b, when the heat diffuses from the initial pump spot, this results in a broadening of the temperature—and thus transient reflectivity—profile. Measuring these profiles for different delay times between the pump and probe pulses enables us to follow in-plane heat diffusion. Due to inefficient out-of-plane thermal transport, the heat can stay in MXene flakes for more than 100 ns,[31] which is longer than the inverse repetition rate of our laser (13 ns). To avoid heat accumulating in the flake, we therefore reduced the repetition rate of the laser by a factor 6 to 10, depending on the flake thickness, using a pulse picker as also discussed in Supporting Information Note 5. For more details on the measurement setup, see Supporting Information Note 2.

Figure 2c shows a typical set of normalized spatial profiles of the transient reflectivity at a few different delay times. We observe that the profiles broaden by ∼50 nm over 4 ns. We are able to resolve this small broadening because, as explained in detail in Supporting Information Note 2.1, our spatial resolution is not limited by the size of the pump and probe, but how stable their size is, alongside how precisely we can position the probe. Through the use of a high-precision scanning mirror, we calculate this to be around ∼7 nm for the probe position at the sample plane. To stabilize the pump and probe widths, we developed an autofocusing procedure which, as described in Supporting Information Note 2.3, provides a beam-width stability of <10 nm over >10 h.

To quantify the broadening of the transient reflectivity profiles, we plot the change in squared width of the profiles $\sigma^2-\sigma_0^2$ as a function of delay time for four different flakes (see Figure 3a and Figure 7 of the Supporting Information for the complete data set). Here, $\sigma$ is the Gaussian width of the profile at a certain delay time and $\sigma_0$ is the width at time-zero, when the pump and probe pulses overlap in time. The slope of the squared width vs time provides the diffusivity $D$, as the solution of the diffusion equation for an initial Gaussian profile is $\sigma^2(\Delta t) = \sigma^2(0) + 2D\Delta t$, where we use the full time delay range


https://doi.org/10.1021/acs.nanolett.6c01850
Nano Lett. XXXX, XXX, XXX−XXX

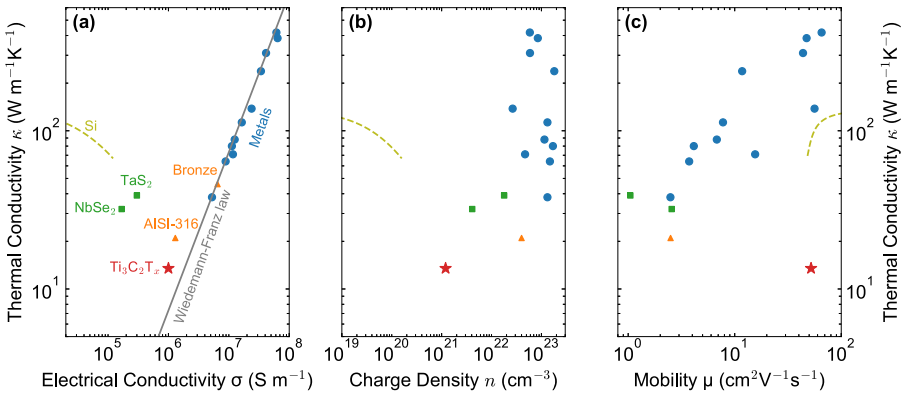


**Figure 4.** Comparison of heat and charge transport properties in different materials. The thermal conductivity as a function of electrical conductivity (a), electron density (b), and electrical mobility (c) of elemental metals (blue ●), from refs 46 and 47, alloys (orange ▲), from ref 48, metallic compounds (green ■), from refs 49 and 50, B-doped silicon with different concentrations (dashed line), from refs 51 and 52, and $Ti_3C_2T_x$ (red ★) (this work and ref 31).

between 30 ps (our time resolution) and 4 ns. Repeating this process for the four different flakes gives an average of $D$ = 0.050 ± 0.002 cm$^2$ s$^{-1}$, resulting in a diffusion length of $L_D$ = 140 nm over 4 ns. This diffusivity is significantly smaller than the thermal diffusivity of few-layer transition metal dichalcogenides ($D$ > 0.15 cm$^2$ s$^{-1}$),[29,30] silicon (0.6 cm$^2$ s$^{-1}$),[36] and gold (1 cm$^2$ s$^{-1}$).[37] This suggests relatively slow in-plane heat transport. We convert the thermal diffusivity to the thermal conductivity $\kappa$ using $\kappa = C_V D$. Here, $C_V$ is the volumetric heat capacity, for which values have been reported between $C_V$ = 2.69 × 10$^6$ J m$^{-3}$ K$^{-1}$[26] and $C_V$ = 3.2 × 10$^6$ J m$^{-3}$ K$^{-1}$;[38] see Supplementary Note 10. This gives an in-plane thermal conductivity of $\kappa$ = 13−16 W m$^{-1}$ K$^{-1}$. Figure 3b shows the obtained thermal conductivities for the four flakes using the $C_V$ from ref 26, giving an average in-plane thermal conductivity of $\kappa$ = 13.5 ± 0.6 W m$^{-1}$ K$^{-1}$.

Before we discuss the relative contributions of electrons and phonons to in-plane heat transport in our MXene flakes, we first describe how ultrafast heat diffusion occurs in typical metals, using gold as an example.[28,37] Initially, photoexcitation introduces energy purely into the electronic system. Through strong electron−electron interactions, within tens of fs, thermal equilibrium within the electron system is established, well before equilibrium with the lattice. As illustrated in Figure 3c, the diffusivity of these hot electrons $D_{hot,el}$ is related to the electronic thermal conductivity $\kappa_{el}$ and the electronic heat capacity $C_{el}$ as $D_{hot,el} = \frac{\kappa_{el}}{C_{el}}$. The thermal conductivity $\kappa_{el}$ is related to the charge conductivity $\sigma_{el}$ via the Wiedemann−Franz law:[39,40] $\kappa_{el} = \frac{\pi^2}{3}\frac{k_B^2}{e^2}T\sigma_{el}$, where $k_B$ is Boltzmann's constant, $e$ is electron charge, and $T$ is temperature. The hot electron diffusivity in this first regime also follows directly from the charge mobility, as we illustrate in Figure 3c and show in Supporting Information Note 9. In gold, the hot-carrier diffusivity in this regime is around 100 cm$^2$ s$^{-1}$.[37]

After some time, the electron and phonon systems have fully equilibrated, and a second regime begins. At this point, the heat is shared between the electron and phonon systems. Thus, as shown in Supporting Information Note 8, the diffusivity is governed by both the electronic and phononic conductivities and heat capacities: $D_{th} = \frac{\kappa_{el}+\kappa_{ph}}{C_{el}+C_{ph}}$, where $\kappa_{ph}$ and $C_{ph}$ are the thermal conductivity and heat capacity of the phonons, respectively. As the heat capacity of phonons is much larger than that of electrons, $C_{ph} \gg C_{el}$, and the electrical conductivity of conventional metals is high, $\kappa_{el} \gg \kappa_{ph}$; this simplifies to $D_{th} \approx \frac{\kappa_{el}}{C_{ph}}$. In gold, the diffusivity observed in this regime is around 1 cm$^2$ s$^{-1}$,[37] which, using its phonon heat capacity, corresponds to the thermal conductivity of gold, which is around 250 W m$^{-1}$ K$^{-1}$.

Returning to our $Ti_3C_2T_x$ MXene flakes, we note that in the first regime, where electrons are not thermalized with the lattice, we expect a diffusivity of the hot electrons of tens of cm$^2$ s$^{-1}$. This value is based on the charge mobility and Fermi level of similar flakes, as obtained using terahertz spectroscopy measurements from ref 31 (see Supporting Information Note 9). Since we observe a much smaller diffusivity in our experiment, we conclude that our measurements correspond to the second regime, where electrons and phonons are in equilibrium. This is also consistent with earlier pump−probe measurements that suggested (sub-)picosecond electron−phonon equilibration,[41] while our time resolution is several tens of picoseconds.

Having established that the obtained diffusivity corresponds to the thermal conduction of equilibrated electrons and phonons, we assess their separate contributions. For the electronic contribution, we use the Wiedemann−Franz law to determine the electronic contribution to the thermal conductivity. For this, we consider a range of charge conductivities of $\sigma_{el}$ = 10$^4$−10$^6$ Sm$^{-1}$. The upper limit is given by the number obtained through all-optical microscopic transport measurements with terahertz pulses[31] and represents a microscopic conductivity that is unaffected by grain boundaries, etc. The lower limit corresponds to values that were obtained using electrical transport measurements in other studies, which can be up to 2 orders of magnitude lower.[42] In particular, studies found conductivities of 9 × 10$^{-5}$ S m$^{-1}$,[43] 4 × 10$^5$ S m$^{-1}$,[44] 5 × 10$^5$ S m$^{-1}$,[16] and 6.5 × 10$^5$ S m$^{-1}$.[45] Using this range of values, the electrical contribution to the thermal conductivity will be at most $\kappa_{el}$ = 7.3 W m$^{-1}$ K$^{-1}$. As illustrated in Figure 3b, this value is significantly lower than our measured thermal conductivity, which is 13−16 W m$^{-1}$ K$^{-1}$. This indicates that phonons must play an important role in the in-plane thermal conductivity of $Ti_3C_2T_x$ MXene. In this analysis, we assumed purely diffusive transport by using a Lorenz number of 1. In ref 19 a violation of the Wiedemann−Franz law was reported, with a Lorenz number of around 0.25 for


https://doi.org/10.1021/acs.nanolett.6c01850
Nano Lett. XXXX, XXX, XXX−XXX

monolayers of $Ti_3C_2T_x$. If similar nondiffusive transport would occur in the thicker flakes that we studied here, the contributions of electrons to heat transport would be four times smaller, meaning that phonons would be an even more dominant carrier of heat.

In typical metals, the thermal conductivity is dominated by electrons, while we found a significant role of phonons for our metallic $Ti_3C_2T_x$ MXene flakes. We illustrate this deviation from the typical metallic behavior in Figure 4a, which shows the thermal conductivity $\kappa$ of several materials as a function of charge conductivity $\sigma_{el}$. Here, we see that the elemental metals nicely follow the Wiedemann−Franz law. Some alloys, two-dimensional metallic compounds, and semiconductors divert from this line, exhibiting a larger thermal conductivity due to phononic contributions. Interestingly, the metallic MXene $Ti_3C_2T_x$ has a unique combination of relatively large charge conductivity with a relatively low thermal conductivity. Making use of the carrier density obtained by THz measurements,[31] in Figure 4b, we compare thermal conductivities as a function of carrier density. Here we find that the reason for the relatively low electronic contribution to the thermal conductivity in $Ti_3C_2T_x$ is the low carrier density of $n = 1.2 \times 10^{21}$ $cm^{-3}$, compared to, for example, $5.9 \times 10^{22}$ $cm^{-3}$ for gold (see Figure 4b). This may relate to predictions of a relatively low density of states—for a metal—around the Fermi level.[53] Figure 4c shows that $Ti_3C_2T_x$ MXene furthermore has a unique combination of relatively large charge mobility and relatively low thermal conductivity. This is different from the case of alloys, where the mobility is reduced due to increased scattering. A better understanding of this combination of properties could be sought through further studies in which, for example, the carrier concentration or mobility of $Ti_3C_2T_x$ is tuned either chemically or externally via gating. Regardless, this comparison shows that $Ti_3C_2T_x$ has an unconventional combination of charge transport and heat transport properties, which is useful for thermal management applications.

In conclusion, we have measured the thermal diffusivity of single multilayer flakes of $Ti_3C_2T_x$ MXene using spatiotemporal microscopy. This technique enabled us to obtain the intrinsic thermal diffusivity without any prior knowledge of material parameters. By measuring single flakes, we eliminated the effects of flake size and interflake thermal resistance. We obtained an in-plane thermal diffusivity of $D = 0.050 \pm 0.002$ $cm^2$ $s^{-1}$, corresponding to a thermal conductivity of $\kappa = 13-16$ W $m^{-1}$ $K^{-1}$. This is comparable to the thermal conductivity measured for other thick flakes,[23] but much higher than for monolayer flakes, where a value of 0.78 W $m^{-1}$ $K^{-1}$ was found. That value is even lower than the value expected based on electron-dominated heat transport following the Wiedemann−Franz law, suggesting a negligible contribution of phonons and nondiffusive electronic heat transport.[19] This suggests a significant dependence of the in-plane thermal conductivity on MXene flake thickness and in particular a strongly decreasing contribution of phonons to heat transport upon approaching the monolayer thickness limit. This requires further research into the thickness dependence of the in-plane thermal conductivity, since differences in termination group composition could also play a role. We compared the upper limit for the electronic contribution to the thermal conductivity, obtained using the electrical conductivity from THz measurements,[31] to the phononic contribution and concluded that phonons play an important role. We then compared the electrical and thermal transport properties to that of other materials and found that the low electronic contribution to the thermal conductivity is not caused by a low mobility, as is the case in alloys and other 2D metallic compounds, but by a relatively low carrier density.

With these in-plane thermal transport measurements, we have shed light on the nature of heat conduction in the $Ti_3C_2T_x$ MXene. Our results show the importance of phonons for in-plane thermal transport, which should be taken into account when designing devices based on these materials. Moreover, the low carrier density could open up ways of tuning the thermal conductivity by changing the carrier density through, e.g., gating or intercalation. This could, for example, be used to create a smart thermal material for active thermal management in electronic devices, batteries, and smart textiles.[54,55]

## ■ ASSOCIATED CONTENT

### Supporting Information

The Supporting Information is available free of charge at https://pubs.acs.org/doi/10.1021/acs.nanolett.6c01850.

Additional details on the experimental methods (Notes 1−7) and theory (Notes 8 and 9), including 7 figures with additional experimental results and descriptions (PDF)

## ■ AUTHOR INFORMATION


### Corresponding Author

**Klaas-Jan Tielrooij** − *Department of Applied Physics and Science Education, Eindhoven University of Technology, Eindhoven 5612 AZ, The Netherlands; Catalan Institute of Nanoscience and Nanotechnology (ICN2), CSIC and BIST, Bellaterra, Barcelona 08193, Spain;* orcid.org/0000-0002-0055-6231; Email: k.j.tielrooij@tue.nl

### Authors

**Max C. van Hemert** − *Department of Applied Physics and Science Education, Eindhoven University of Technology, Eindhoven 5612 AZ, The Netherlands;* orcid.org/0009-0005-4791-2204

**Hugh Ramsden** − *Department of Applied Physics and Science Education, Eindhoven University of Technology, Eindhoven 5612 AZ, The Netherlands*

**Stefano Ippolito** − *A.J. Drexel Nanomaterials Institute and Department of Materials Science and Engineering, Drexel University, Philadelphia, Pennsylvania 19104, United States*

**Sebin Varghese** − *Department of Applied Physics and Science Education, Eindhoven University of Technology, Eindhoven 5612 AZ, The Netherlands*

**Bohai Liu** − *Department of Applied Physics and Science Education, Eindhoven University of Technology, Eindhoven 5612 AZ, The Netherlands*

**Elvira Tornero Gasca** − *Energy2Devices, Instituto de Ciencia de Materiales de Madrid (ICMM), Madrid 28049, Spain*

**Miguel Muñoz Rojo** − *Energy2Devices, Instituto de Ciencia de Materiales de Madrid (ICMM), Madrid 28049, Spain; Department of Thermal and Fluid Engineering, Faculty of Engineering Technology, University of Twente, Enschede 7500 AE, The Netherlands;* orcid.org/0000-0001-9237-4584

**Hai I. Wang** − *Max Planck Institute for Polymer Research, Mainz 55128, Germany; Debye Institute for Nanomaterials*






https://doi.org/10.1021/acs.nanolett.6c01850
Nano Lett. XXXX, XXX, XXX−XXX

*Science, Utrecht University, Utrecht 3584, The Netherlands;* orcid.org/0000-0003-0940-3984

**Yury Gogotsi** − *A.J. Drexel Nanomaterials Institute and Department of Materials Science and Engineering, Drexel University, Philadelphia, Pennsylvania 19104, United States;* orcid.org/0000-0001-9423-4032

Complete contact information is available at: https://pubs.acs.org/10.1021/acs.nanolett.6c01850

## Notes

The authors declare no competing financial interest.

## ■ ACKNOWLEDGMENTS

The authors thank Changhoon Park for discussions. The ICN2 is supported by the Severo Ochoa Centres of Excellence program, Grant CEX2021-001214-S, funded by MCIU/AEI/10.13039.501100011033. K.-J.T. acknowledges funding from the European Union's Horizon 2020 research and innovation program under Grant Agreement No. 101125457 (ERC CoG "EQUATE") and Spanish MCIN/AEI project (PID2022-142730NB-I00 "HYDROPTO"). M.M.R. acknowledges the European Union ERC CoG THERMO2DEAL 101123381, the national project MXENE2DEVICES (PID2023-149764OA-I00), and the Severo Ochoa Centres of Excellence program through Grant CEX2024-001445-S. S.I. and Y.G. acknowledge the Army Research Laboratory for supporting this work under Cooperative Agreements no. W911NF-19-2-0119 and W911NF-24-2-0100.

## ■ REFERENCES

(1) Naguib, M.; Kurtoglu, M.; Presser, V.; Lu, J.; Niu, J.; Heon, M.; Hultman, L.; Gogotsi, Y.; Barsoum, M. W. Two-Dimensional Nanocrystals Produced by Exfoliation of $Ti_3AlC_2$. *Adv. Mater.* **2011**, *23* (37), 4248−4253.

(2) Naguib, M.; Mochalin, V. N.; Barsoum, M. W.; Gogotsi, Y. 25th Anniversary Article: MXenes: A New Family of Two-Dimensional Materials. *Adv. Mater.* **2014**, *26* (7), 992−1005.

(3) Nashim, A.; Parida, K. A Glimpse on the plethora of applications of prodigious material MXene. *Sustainable Materials and Technologies* **2022**, *32*, No. 00439.

(4) Yadav, M.; Kumar, M.; Sharma, A. Review of $Ti_3C_2T_x$ MXene Nanosheets and their Applications. *ACS Applied Nano Materials* **2024**, *7* (9), 9847−9867.

(5) Wu, Y.; Sun, M. Recent progress of MXene as an energy storage material. *Nanoscale Horizons* **2024**, *9* (2), 215−232.

(6) Thakur, A.; Zhang, Y.; Gogotsi, Y.; Anasori, B. Electrochemistry of MXenes and their sustainable energy applications. *MRS Energy & Sustainability* **2025**, *12* (2), 270−282.

(7) Hassan, T.; Park, C.; Naqvi, S. M.; Kim, J.; Kim, H.; Khalid, Z.; Jung, S.; Gogotsi, Y.; Koo, C. M. MXenes for Infrared Thermal Management. *ACS Nano* **2025**, *19* (48), 40703−40732.

(8) Iqbal, A.; Hassan, T.; Naqvi, S. M.; Gogotsi, Y.; Koo, C. M. MXenes for multispectral electromagnetic shielding. *Nature Reviews Electrical Engineering* **2024**, *1* (3), 180−198.

(9) Zhang, Z.; Tao, C.; Yin, H.; Nie, W.; Duan, J.; Huang, Y.; Wang, X. MXene materials: Developments and sensor applications in modern infrastructure. *J. Mater. Sci.* **2025**, *60* (28), 11744−11777.

(10) Nagaraja, T.; Thakur, A.; Krayev, A.; Robinson, A. E.; Vojvodic, A.; Anasori, B.; Das, S. R. MXene electrochemical phosphate sensors. *Communications Engineering* **2025**, *4* (1), 189.

(11) Rouhi, S.; Bay, M.; Aydin, O.; Sicim, E. S.; Ay, F.; Perkgoz, N. K. Large-area growth of $Mo_2C$ thin films and MXene structures via the PVD-CVD hybrid technique. *New J. Chem.* **2025**, *49* (24), 10194−10204.

(12) Antony Jose, S.; Price, J.; Lopez, J.; Perez-Perez, E.; Menezes, P. L. Advances in MXene Materials: Fabrication, Properties, and Applications. *Materials* **2025**, *18* (21), 4894.

(13) Ren, W.; Boggild, P.; Redwing, J. M.; Novoselov, K. S.; Sun, L.; Qi, Y.; Jia, K.; Liu, Z.; Burton, O.; Alexander-Webber, J. A.; Hofmann, S.; Cao, Y.; Long, Y.; Yang, Q.-H.; Li, D.; Choi, S. H.; Kim, K. K.; Lee, Y. H.; Li, M.; Huang, Q.; Gogotsi, Y.; Clark, N.; Carl, A.; Gorbachev, R.; Olsen, T.; Rosen, J.; Thygesen, K. S.; Efetov, P. D. D. K.; Jessen, B. S.; Yankowitz, M.; Barrier, J.; Kumar, R. K.; Koppens, F.; Deng, H.; Li, X.; Dai, S.; Basov, D.; Wang, X.; Das, S.; Duan, X.; Yu, Z.; Borsch, M.; Ferrari, A. C.; Huber, R.; Kira, M.; Xia, F.; Wang, X.; Wu, Z.-S.; Feng, X.; Simon, P.; Cheng, H.-M.; Liu, B.; Xie, Y.; Jin, W.; Nair, R. R.; Xu, Y.; Zhang, H.-B.; Pellegrini, V.; Qu, B.; Lemme, M.; Katiyar, A.; Ahn, J.-H.; Aharonovich, I.; Hersam, M. C.; Roche, S.; Hua, Q.; Shen, G.; Ren, T.-L.; Koo, C. M.; Koratkar, N. A.; Young, R. J.; Pollard, A. The 2D Materials Roadmap. *2D Materials* **2026**, *13*, 021501.

(14) Caffrey, N. M. Effect of mixed surface terminations on the structural and electrochemical properties of two-dimensional $Ti_3C_2T_2$ and $V_2CT_2$ MXenes multilayers. *Nanoscale* **2018**, *10* (28), 13520−13530.

(15) Fatima, J.; Tahir, M. B.; Rehman, M. A.; Assiri, M. A.; Imran, M.; Alzaid, M.; Alrobei, H. Structural, optical and electronic properties of novel 2D carbides and nitrides MXene based Materials: A DFT study. *Optical and Quantum Electronics* **2023**, *55* (7), 576.

(16) Lipatov, A.; Bagheri, S.; Sinitskii, A. Metallic Conductivity of $Ti_3C_2T_x$ MXene Confirmed by Temperature-Dependent Electrical Measurements. *ACS Materials Letters* **2024**, *6* (1), 298−307.

(17) Chen, L.; Shi, X.; Yu, N.; Zhang, X.; Du, X.; Lin, J. Measurement and Analysis of Thermal Conductivity of $Ti_3C_2T_x$ MXene Films. *Materials* **2018**, *11* (9), 1701.

(18) Wu, H.; Gu, J.; Li, Z.; Liu, W.; Bao, H.; Lin, H.; Yue, Y. Characterization of phonon thermal transport of $Ti_3C_2T_x$ MXene thin film. *J. Phys.: Condens. Matter* **2022**, *34* (15), No. 155704.

(19) Huang, Y.; Spiece, J.; Parker, T.; Lee, A.; Gogotsi, Y.; Gehring, P. Violation of the Wiedemann-Franz Law and Ultralow Thermal Conductivity of $Ti_3C_2T_x$ MXene. *ACS Nano* **2024**, *18* (47), 32491−32497.

(20) Liu, R.; Li, W. High-Thermal-Stability and High-Thermal-Conductivity $Ti_3C_2T_x$ MXene/Poly(vinyl alcohol) (PVA) Composites. *ACS Omega* **2018**, *3* (3), 2609−2617.

(21) Yu, L.; Huang, D.; Wang, X.; Yu, W.; Yue, Y. Tuning thermal and electrical properties of MXenes via dehydration. *Phys. Chem. Chem. Phys.* **2022**, *24* (42), 25969−25978.

(22) Liu, Y.; Wu, Y.; Wang, X. Thermal transports in the MXenes family: Opportunities and challenges. *Nano Research* **2024**, *17* (8), 7700−7716.

(23) Kumari, K.; Thiyagarajan, R.; Kale, A. J.; Batra, R.; Krishanmurty, S.; Sethupathi, K.; Rao, M. S. R. Probing phonon anharmonicity of multilayer $Ti_3C_2T_x$, (T: OH, O, or F) MXene through temperature- and pressure-dependent Raman studies. *Phys. Rev. B* **2025**, *111* (11), No. 115411.

(24) Ippolito, S.; Urban, F.; Samorì, P.; Spanier, J. E.; Gogotsi, Y. Exotic Photothermal Response in Ti-Based MXene Optoelectronic Devices. *Advanced Electronic Materials* **2025**, *11* (13), No. 2500017.

(25) De Leuze, O.; Fernandes, F. M.; Arib, S.; Caputo, L.; Fontes, A. P.; Nguyen, V.-H.; Pazniak, H.; Nysten, B.; Charlier, J.-C.; Hermans, S.; Hackens, B. Anisotropic charge transport in 2D single crystals of $Ti_3C_2T_x$ MXenes. *Communications Materials* **2025**, *6* (1), 186.

(26) Tornero Gasca, E.; Liu, B.; Ippolito, S.; van Hemert, M. C.; Ramsden, H.; Saleta Reig, D.; Schmidt, A. J.; Ramos Jimenez, M.; Klinar, K.; Gogotsi, Y.; Tielrooij, K.-J.; Muñoz Rojo, M. Temperature-dependent and thickness-independent out-of-plane heat transport of two-dimensional $Ti_3C_2T_x$ MXene flakes. Submitted (**2026**).

(27) Vazquez, G. D. B.; Morganti, G. L. G.; Block, A.; Van Hulst, N. F.; Liebel, M.; Tielrooij, K.-J. Spatiotemporal Microscopy: Shining Light on Transport Phenomena. *Advanced Electronic Materials* **2024**, *10*, No. 2300584.

(28) Block, A.; Yu, R.; Un, I.-W.; Varghese, S.; Liebel, M.; Van Hulst, N. F.; Fan, S.; Tielrooij, K.-J.; Sivan, Y. Observation of Negative Effective Thermal Diffusion in Gold Films. *ACS Photonics* **2023**, 2−01916.
(29) Varghese, S.; Mehew, J. D.; Block, A.; Reig, D. S.; Woźniak, P.; Farris, R.; Zanolli, Z.; Ordejón, P.; Verstraete, M. J.; Van Hulst, N. F.; Tielrooij, K.-J. A pre-time-zero spatiotemporal microscopy technique for the ultrasensitive determination of the thermal diffusivity of thin films. *Rev. Sci. Instrum.* **2023**, *94* (3), No. 034903.
(30) Weaver, H. L.; Went, C. M.; Wong, J.; Jasrasaria, D.; Rabani, E.; Atwater, H. A.; Ginsberg, N. S. Detecting, Distinguishing, and Spatiotemporally Tracking Photogenerated Charge and Heat at the Nanoscale. *ACS Nano* **2023**, *17* (19), 19011−19021.
(31) Zheng, W.; Ramsden, H.; Ippolito, S.; van Hemert, M.; Zhang, D.; Zhang, T.; Li, D.; Wen, G.; Geuchies, J.; Yu, M.; Feng, X.; Gogotsi, Y.; Tielrooij, K.-J.; Wang, H. I. Photothermal effects control ultrafast charge transport in titanium carbide MXenes. *Nat. Commun.* **2026**, *17*, 1201.
(32) Downes, M.; Shuck, C. E.; McBride, B.; Busa, J.; Gogotsi, Y. Comprehensive synthesis of $Ti_3C_2T_x$ from MAX phase to MXene. *Nat. Protoc.* **2024**, *19* (6), 1807−1834.
(33) Leung, P. T.; et al. Surface-enhanced Raman scattering at elevated temperatures. *Phys. Rev. B* **1996**, *53* (19), 12659−12662.
(34) Maleski, K.; Shuck, C. E.; Fafarman, A. T.; Gogotsi, Y. The Broad Chromatic Range of Two-Dimensional Transition Metal Carbides. *Advanced Optical Materials* **2021**, *9* (4), No. 2001563.
(35) Colin-Ulloa, E.; Fitzgerald, A.; Montazeri, K.; Mann, J.; Natu, V.; Ngo, K.; Uzarski, J.; Barsoum, M. W.; Titova, L. V. Ultrafast Spectroscopy of Plasmons and Free Carriers in 2D MXenes. *Adv. Mater.* **2023**, *35* (8), No. 2208659.
(36) Delor, M.; Weaver, H. L.; Yu, Q.; Ginsberg, N. S. Imaging material functionality through three-dimensional nanoscale tracking of energy flow. *Nat. Mater.* **2020**, *19* (1), 56−62.
(37) Block, A.; Liebel, M.; Yu, R.; Spector, M.; Sivan, Y.; García de Abajo, F. J.; van Hulst, N. F. Tracking ultrafast hot-electron diffusion in space and time by ultrafast thermomodulation microscopy. *Science Advances* **2019**, *5* (5), 8965.
(38) Srivatsa, S.; Tokarz, W.; Przewoźnik, J.; Strączek, T.; Grabowski, K.; Rutkowski, P.; Uhl, T.; Kulawik, J.; Kata, D.; Madej, D.; Lis, J.; Kapusta, C. Temperature Evolution of Composition, Thermal, Electrical and Magnetic Properties of $Ti_3C_2T_x$ -MXene. *Materials* **2024**, *17* (10), 2199.
(39) Franz, R.; Wiedemann, G. Über die Wärme-Leitungsfähigkeit der Metalle. *Annalen der Physik* **1853**, *165* (8), 497−531.
(40) Lorenz, L. Bestimmung der Wärmegrade in absolutem Maasse. *Annalen der Physik* **1872**, *223* (11), 429−452.
(41) Zhang, Q.; Li, J.; Wen, J.; Li, W.; Chen, X.; Zhang, Y.; Sun, J.; Yan, X.; Hu, M.; Wu, G.; Yuan, K.; Guo, H.; Yang, X. Simultaneous capturing phonon and electron dynamics in MXenes. *Nat. Commun.* **2022**, *13* (1), 7900.
(42) Spies, J. A.; Neu, J.; Tayvah, U. T.; Capobianco, M. D.; Pattengale, B.; Ostresh, S.; Schmuttenmaer, C. A. Terahertz Spectroscopy of Emerging Materials. *J. Phys. Chem. C* **2020**, *124* (41), 22335−22346.
(43) Lipatov, A.; Goad, A.; Loes, M. J.; Vorobeva, N. S.; Abourahma, J.; Gogotsi, Y.; Sinitskii, A. High electrical conductivity and breakdown current density of individual monolayer $Ti_3C_2T_x$ MXene flakes. *Matter* **2021**, *4* (4), 1413−1427.
(44) Lipatov, A.; Alhabeb, M.; Lukatskaya, M. R.; Boson, A.; Gogotsi, Y.; Sinitskii, A. Effect of Synthesison Quality, Electronic Properties and Environmental Stability of Individual Monolayer $Ti_3C_2$ MXene Flakes. *Advanced Electronic Materials* **2016**, *2* (12), No. 1600255.
(45) Shekhirev, M.; Busa, J.; Shuck, C. E.; Torres, A.; Bagheri, S.; Sinitskii, A.; Gogotsi, Y. Ultralarge Flakes of $Ti_3C_2T_x$ MXene via Soft Delamination. *ACS Nano* **2022**, *16* (9), 13695−13703.
(46) Ashcroft, N. W.; Mermin, N. D. *Solid State Physics*; Saunders College, Philadelphia, (1976). Chapter xxi.
(47) Kaye, G. W. C.; Laby, T. H. *Tables of Physical and Chemical Constants*, 1.0 ed.; Kaye & Laby Online, Middlesex, 2005.
(48) Goodfellow: High-Quality Alloys for Advanced Applications | Goodfellow. https://www.goodfellow.com/eu/material/alloys.
(49) Zhu, T.; Litwin, P. M.; Rosul, M. G.; Jessup, D.; Akhanda, M. S.; Tonni, F. F.; Krylyuk, S.; Davydov, A. V.; Reinke, P.; McDonnell, S. J.; Zebarjadi, M. Transport properties of few-layer $NbSe_2$: From electronic structure to thermoelectric properties. *Materials Today Physics* **2022**, *27*, No. 100789.
(50) Wang, S.; Yang, X.; Hou, L.; Cui, X.; Zheng, X.; Zheng, J. Organic covalent modification to improve thermoelectric properties of $TaS_2$. *Nat. Commun.* **2022**, *13* (1), 4401.
(51) Masetti, G.; Severi, M.; Solmi, S. Modeling of carrier mobility against carrier concentration in arsenic-, phosphorus-, and boron-doped silicon. *IEEE Trans. Electron Devices* **1983**, *30* (7), 764−769.
(52) Lee, Y.; Hwang, G. S. Mechanism of thermal conductivity suppression in doped silicon studied with nonequilibrium molecular dynamics. *Phys. Rev. B* **2012**, *86* (7), No. 075202.
(53) Enyashin, A. N.; Ivanovskii, A. L. Two-dimensional titanium carbonitrides and their hydroxylated derivatives: Structural, electronic properties and stability of MXenes $Ti_3C_{2-x}N_x$, $(OH)_2$ from DFTB calculations. *J. Solid State Chem.* **2013**, *207*, 42−48.
(54) Zhang, Z.; Cao, B. Thermal smart materials with tunable thermal conductivity: Mechanisms, materials, and applications. *Science China Physics, Mechanics & Astronomy* **2022**, *65* (11), No. 117003.
(55) Hartquist, C. M.; Li, B.; Zhang, J. H.; Yu, Z.; Lv, G.; Shin, J.; Boriskina, S. V.; Chen, G.; Zhao, X.; Lin, S. Reversible two-way tuning of thermal conductivity in an end-linked star-shaped thermoset. *Nat. Commun.* **2024**, *15* (1), 5590.